Computers and Fluids 126 (2016) 181–191

Contents lists available at ScienceDirect

Computers and Fluids

journal homepage: www.elsevier.com/locate/compfluid

Assessment of turbulence model performance: Severe acceleration with large integral length scales

Xiaoyu Yang*, Paul G. Tucker

Department of Engineering, University of Cambridge, Trumpington Street, Cambridge CB2 1PZ, United Kingdom

ARTICLE INFO

Article history:
Received 15 December 2014
Revised 8 September 2015
Accepted 24 November 2015
Available online 17 December 2015

Keywords:
Turbulence
Turbulence modelling
Acceleration
Reynolds-stress models
Eddy-viscosity models
Reynolds-averaged Navier–Stokes simulation
Computational Fluid Dynamics

ABSTRACT

Turbulence is substantially laminarised, when the mean flow experiences streamwise acceleration above a certain critical acceleration parameter. Recently, to essentially reveal aero engine intake acceleration scenarios, Direct Numerical Simulations (DNS) have been performed for turbulent flow through a rapidly contracting channel. On average, the streamwise acceleration parameter K_s is of the magnitude of 1×10^{-5}. Converged statistics show that it is the streamwise acceleration that causes the first term of the production rate for $\overline{u'u'}$ to be negative. This initiates the degeneration towards laminar flow and also closes the usual wall turbulence self-sustaining mechanism. Further downstream, the progressive turbulence recovery is largely streamwise dominant. Importantly, the laminarisation effects are lagging to the rate of contraction. To assess the corresponding turbulence model performance and for better modelling, for the same flow configurations, Reynolds-averaged Navier–Stokes (RANS) predictions are compared, using some available Reynolds-stress (RSM) and eddy-viscosity models. These are the second-order closure with the strain–ω formulation, the standard k–ω and the Menter's shear-stress transport (SST) models, the standard Spalart–Allmaras (S–A) model, and that with the strain–vorticity correction. As will be shown, through the contraction, all the benchmarked models are able to predict the essential characteristics of the laminarisation; whereas, further downstream, the eddy-viscosity models tend to return the flow immediately back to the fully developed turbulence. In contrast, the RSM predicts the gradually recovery process, in spite of the lower growth rate, relative to that of the DNS. The S–A model has been modified for the lagging mechanism caused by severe acceleration. The corresponding modified predictions better match the mean flow characteristics. Moreover, all models would also benefit from sensitisation to the impact of the large integral length scales.

1. Introduction

Degeneration towards laminar flow occurs, when a turbulent boundary layer (TBL) continues experiencing a substantial acceleration field for sufficient distance [1–12]. This is usually produced from a strong favourable pressure gradient. The early measurements, investigated by Launder and Jones [1,2,13–15], show that laminarisation is of significance, when the streamwise acceleration parameter

$$K_s \equiv \frac{\nu_0}{U_e^2}\frac{dU_e}{ds} \equiv -\frac{\nu_0}{\rho U_e^3}\frac{dp}{ds} \tag{1}$$

exceeds a value of about 2×10^{-6}. However, only for $K_s \gtrsim 1 \times 10^{-5}$, the reversion to laminar is seemingly complete. This case is considered as a "severe" acceleration. Otherwise, the boundary layer is partially laminarised, as it experiences is a "moderate" acceleration. Importantly, the laminarisation effects lag the acceleration. For example, with $K_{s,max} \simeq 1.5 \times 10^{-5}$, downstream of the acceleration, the shape factor H_{shape} rises dramatically above the laminar value of 2.0 [1]. Also, as visualised by Schraub and Kline [3], for an accelerated boundary layer, the low-speed-streaks (LSS) — the signature of TBL — do not suddenly disappear from the sublayer. Moreover, for three moderate accelerations, 0.7×10^{-6}, 1.3×10^{-6}, and 3.0×10^{-6}, Launder and Stinchcombe [16] observed a substantial self-preserving u' component within partially laminarised boundary layers. In this situation, the boundary layer is still essentially turbulent, but with distinct features. When determining the onset of laminarisation, a local acceleration parameter, defined as $L_K \equiv K_s \cdot C_f^{-3/2} \equiv -(\nu_0/\rho u_\tau^3) \cdot dp/ds$, is frequently examined [2,7].

As a particular subset of the above research, a sink flow TBL/two-dimensional convergent channel is of special relevance to study laminarisation [1,2,17]. Asymptotically, in these self-preserving equilibrium flows, K_s is a constant from station to station; moreover, for a given value of K_s, the friction coefficient C_f, the Reynolds numbers of the displacement δ^* and momentum θ thickness, and also the shape

* Corresponding author. Tel.: +44 1223 337 582; fax: +44 1223 332 662.
E-mail address: xiaoyu.yang@alumni.stanford.edu, xiaoyu.yang.alumni.cambridge@outlook.com (X. Yang).

http://dx.doi.org/10.1016/j.compfluid.2015.12.007

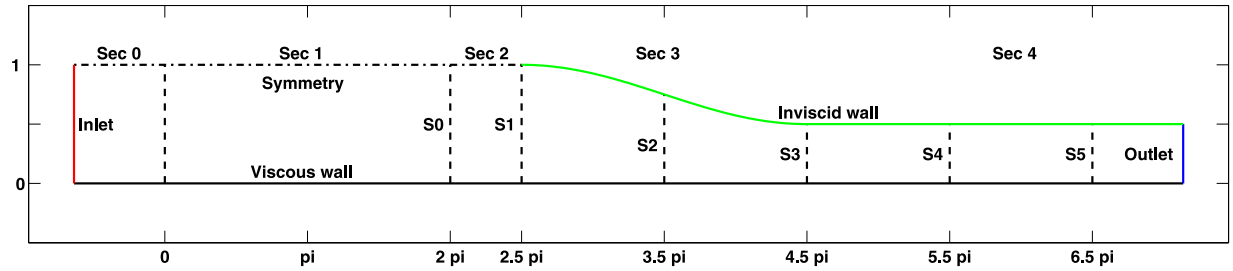

Fig. 1. Schematic of the lower half of the actual simulated contraction channel. (Note: the streamwise lengths for the upstream inlet section (Sec 0) and the downstream outlet section (Sec 4) are 120δ and 30δ, respectively. These are not shown in the figure. Also, the half-channel height δ is scaled to be unity, and the axes are not equal.)

factor H_{shape} are all independent of the streamwise coordinate. For this, Direct Numerical Simulations (DNS) with K_s between 1.5×10^{-6} and 3.0×10^{-6} are presented in similarity coordinates by Spalart [18].

For early attempts to numerically predict moderate laminarisation effects [1,2], the Prandtl mixing-length hypothesis [19,20] is exploited, together with the Van Driest recommendation [21] for the mixing-length/effective-viscosity distribution at the near wall region. Particularly, in these predictions, the damping function A^+ is modified as a function of K_s, instead of the original constant of 26. Comparisons with measurements are encouraging. Meanwhile, for severe acceleration, the turbulent shear stress is assumed to be constant along a streamline by Launder and Jones [1]. This "frozen" hypothesis leads to reasonably accurate predictions of the momentum thickness θ and the shape factor H_{shape} [1]. Similarly, based on the mixing-length concept, other efforts are made, for example, by Kays et al. [22], Cebeci and Mosinskis [23], and Powell and Strong [24].

Using the k–ϵ model, Jones and Launder [25] and Launder and Spalding [26,27] predicted equilibrium sink flow behaviour ($K_s \simeq 2.2 \times 10^{-6}$) and also heat transfer through non-equilibrium accelerated boundary layers ($K_s = 2.0 \times 10^{-6} \sim 7.0 \times 10^{-6}$). Overall, the $k-\epsilon$ model in its low Reynolds number form is remarkably successful. However, it was noticed that, further downstream, the model exhibited a substantially higher recovery rate of heat transfer coefficient than measurements after the acceleration/pressure gradient ceased.

Moreover, for turbulence models, such as the k–ϵ model based on the effective-viscosity concept, the transport effects for turbulent stresses, particularly for the shear stress within boundary layer flows, are not replicated well. To deal with this, a Reynolds-stress model (RSM), with the scale-determining ϵ equation similar in some respects to the above used by Jones and Launder, is systematically derived by Hanjalic and Launder [28,29]. Encouraging agreement with measurements for an equilibrium sink flow ($K_s \simeq 1.5 \times 10^{-6}$) [17], and more importantly for a non-equilibrium flat-plate boundary layer with severe acceleration ($K_s \simeq 3.0 \times 10^{-5}$) [13] are found.

Later numerical and experimental developments are well introduced by Piomelli and Yuan [30], where DNS and Large Eddy Simulations (LES) are presented for spatially developing boundary layers, subject to accelerations strong enough to cause laminarisation. Meanwhile, the developments of turbulence modelling for Reynolds-averaged Navier–Stokes simulations (RANS) of accelerating boundary layers are introduced, for example, by Karimisani et al. [31] and Oriji and Tucker [32]. The latter focuses on aero engine intakes.

To essentially reveal such intake acceleration scenarios, the course of laminarisation is directly simulated through a rapidly contracting channel with various contraction ratios and lengths in [33]. Relatively large integral turbulence length scales such as might be found in atmospheric turbulence are considered. Accordingly, the peak acceleration parameter $K_{s,\,max}$ varies from 0.977×10^{-5} to 5.594×10^{-5}. This level of acceleration is also of strong potential importance commonly arising in flows through rocket nozzles and turbine blades [1,25].

As has been shown [33], it is the presence of the streamwise acceleration ($\partial U/\partial s > 0$, where s is the streamwise coordinate) that causes the first term of the production rate of $\overline{u'u'}$ to be destructive; this initiates the degeneration towards laminar flow. Consequently, this closes the usual wall turbulence self-sustaining mechanism based on the transverse mean shear. In this process, the pressure redistribution terms progressively vanish through the contraction and thereafter. Therefore, further downstream after the strong favourable pressure gradient, turbulence is gradually recovered but into substantially streamwise dominant structures. Consequently, $\overline{u'u'}$ recovers gradually, whereas $\overline{v'v'}$ and $\overline{w'w'}$ stay at their minimum levels, nearly the same as those when leaving the contraction. Accordingly, if scaled by the corresponding inner values, it can be seen that the above production rate term, i.e. $\frac{1}{2}P^+_{11,a} = -\overline{u'u'}^+ \cdot K_s^+$, directly quantifies the destruction rate of TKE; also, $\frac{1}{2}P^E_{11,a} = -(\overline{u'u'}/U^2_{edge}) \cdot K_s^E$ provides such a measure in the outer scale; whereas, $K_s^+ = (\partial U/\partial s)/(\partial U/\partial n)_w$ and $K_s^E = (\nu_0/U^2_{edge}) \cdot (\partial U/\partial s)$ generally reflect the significance of *the destruction rate* (s and n are the corresponding streamwise and wall-normal coordinates.) Moreover, the streamwise length L_s of the acceleration field is another important parameter for the laminarisation process [1,13,14,33]. As suggested by K_s^E, when the TKE destruction rates are similar, the laminarisation process is more complete for the cases experiencing longer acceleration distance/period. Importantly, the laminarisation effects are lagging to the contraction influence; after the severe acceleration, H_{shape} can rise above the theoretical laminar solution of 2.0. These recent observations above are of fundamental significance for aero engine intake flow physics, as well as many other aerospace applications. For better turbulence modelling, RANS predictions are also calculated for the same flow configuration as Case I(x) ($K_{s,max} = 4.860 \times 10^{-5}$) of the DNS [33], using some popular Reynolds-stress and eddy-viscosity models available to the current study.

2. Numerical methods

The detailed descriptions on these selected models and the corresponding numerical procedure, using compressible Rolls-Royce HYDRA [34,35] and incompressible ANSYS-FLUENT (Version 13) [36], have been given in the other paper [37]. Notably, for the former, a second order Roe's scheme with a low Ma number preconditioning is employed for spatial discretisation. The four-stage Runge–Kutta time integration, together with a four-level multi-grid cycle, is used to approach a steady state solution. For FLUENT, the steady state is approached through the pseudo-transient time integration; the least-square cell based gradient term, the second-order pressure term, and the third-order MUSCL scheme for the momentum and other turbulence-model terms is employed. These benchmarked models in their low Reynolds number forms are the second-order closure with the stress–ω formulation, the standard k–ω and the SST models, the standard S–A model and that with the strain–vorticity correction. Moreover, as shown in Fig. 1 for the schematic of the lower half-channel, the standard no-slip wall boundary condition is applied to the exterior viscous channel wall, with the viscous sublayer directly resolved. The standard inviscid wall boundary condition is

applied to the interior wall. This will be further discussed shortly. Additionally, the stagnation and static pressure difference, through the standard pressure inlet boundary condition, is used to drive the inflow, to match the desired flow properties at the upstream fully developed region; and the standard outflow boundary condition is applied to the channel exit. For all the following results, the iterative convergence criteria is taken to be 1×10^{-6} for all the scaled residuals.

Importantly, as will be shown in the following, for all the benchmarked models, the predictive error progressively arises through the severe acceleration. For this, to match the DNS data, the standard S–A model [38] without transition terms, i.e. Eq. (2) with $\sigma^a_{K_s} = 1$ and $\sigma^b_{K_s} = 1$, is modified as follows: downstream to a severe acceleration ($K_{s,max} \simeq 1.0 \times 10^{-5}$), the production and dissipation mechanism is switched off, and the corresponding viscous and turbulent diffusion is substantially reduced by a factor of 0.1, i.e. $\sigma^a_{K_s} = 0$ and $\sigma^b_{K_s} = 0.1$. This modified model equation has the form

$$\frac{D\tilde{\nu}}{Dt} = \sigma^a_{K_s}\{P_{S-A} - \epsilon_{S-A}\} + \frac{\sigma^b_{K_s}}{\sigma}\{\nabla \cdot [(\tilde{\nu} + \nu)\nabla\tilde{\nu}] + C_{b2}(\nabla\tilde{\nu}) \cdot (\nabla\tilde{\nu})\}. \tag{2}$$

where the production and dissipation terms for the S–A model are $P_{S-A} = C_{b1}\tilde{S}\tilde{\nu}$ and $\epsilon_{S-A} = C_{w1} f_w (\tilde{\nu}/d)^2$. Also, ν and $\tilde{\nu}$ are the molecular and the modified turbulent viscosities, respectively. For a detailed description of the modelled functions and parameters, see Spalart and Allmaras [38]. The constants used in the above modifications essentially render production, dissipation, and diffusion inactive to reflect a frozen turbulence state. Hence, the values themselves are general if applied to turbulence in the frozen state. Evaluation of the acceleration parameter in a complex geometry application with an unstructured flow solver is outlined in Oriji and Tucker [32].

3. Flow configuration

For the current RANS simulations, the two-dimensional contraction channel is the same as the cross-section of the DNS case. It contains an upstream fully developed section (Sec 1), an immediate upstream guide section (Sec 2), and also a contraction section (Sec 3). The streamwise lengths for these sections are $L_1 = 2\pi\delta$, $L_2 = 0.5\pi\delta$, and $L_3 = 2\pi\delta$; where δ is the upstream half-channel height. Additionally, a most upstream inlet section (Sec 0 with $L_0 = 120\delta$) is used to fully develop the flow, as well as a parallel outlet section (Sec 4 with $L_4 = 30\delta$) for outflow. Also, to accelerate the flow separately, starting from the channel centreline at the leading edge of the contraction, the channel is split into the top and bottom halves through the cosine shaped contraction, respectively. The schematic of the lower half-channel is given in Fig. 1. The contraction ratio h_4/h_1 is 0.5; where h_4 and h_1 are the corresponding geometrical half-channel heights. Accordingly, inviscid wall boundary condition is applied to the corresponding interior channel surfaces; whereas, the standard viscous wall boundary condition is used for all the other exterior surfaces. Notably, the coordinate origin is on the lower viscous wall $2.5\pi\delta$ upstream to the leading edge of the contraction. It is at the end of the RANS inlet section (Sec 0). In this way, the coordinates are exactly the same as for the DNS case. Similarly, the flow is simulated at nominally $Re_\delta = 3300$, or equivalently $Re_\tau \simeq 180$. For the upstream fully developed flow, the half-channel height h, or equivalently the boundary layer thickness δ, is kept as 1 mm; under sea-level atmospheric condition, this requires the centreline velocity $U_{max} = 48.262$ m/s, i.e. $Ma \simeq 0.142$. Additionally, for the five streamwise sections above, the grid resolution is $(31, 25, 7, 16, 31) \times 51$. Also, for the upstream sections, the first grid spacing above the viscous walls is $\Delta d/h_1 = 0.002$, or equivalently $\Delta d^+_{1st} \sim 0.36$ resolving the viscous sublayer. A grid independence study shows that the average profile change for the mean velocities is less than 0.1% and the change in turbulence quantities around 1% for a grid doubled in all directions. This is for the RSM which is expected to have the greatest sensitivity to grid. For the models involving less equations and hence gradients, smaller changes are expected. In the following, only the results close to the contraction (Sections 2, 3, and the leading part of 4) will be examined. Besides, in the following, x, y, and z will be used as the streamwise, wall-normal, and spanwise coordinates, respectively. In the following, the benchmark results are examined. These include the mean velocity profiles, the streamwise distributions of C_f and C_p, and the characteristics of TKE, K^E_s, and K^+_s distributions. The definition for these parameters will be given in the following.

Table 1
Streamwise distance (s/δ) to the leading edge of the contraction.

Stations	s/δ[a]
$S0$	-0.5π
$S1$	0
$S2$	π
$S3$	2π
$S4$	3π
$S5$	4π

[a] The axes origin is $2.5\pi\delta$ upstream to the leading edge of the contraction, and it is on the lower viscous wall.

4. Discussion of results

Figs 2–4 compare these RANS predictions with the DNS for the mean velocity wall-normal distributions at six streamwise stations. These are given in the frame (a) of Fig. 2 to the frame (b) of Fig. 4, respectively. The streamwise locations of these stations have been shown in Fig. 1. The first four locations (S0–S3) are upstream of, the leading edge, the mid-plane, and the trailing edge of the contraction, and the other two (S4 and S5) are located further downstream. The corresponding streamwise distances to the leading edge of the contraction are given in Table 1. Also, in these figures, the wall-normal distance is scaled by the corresponding local half-channel height, and the mean velocity by the centreline value of the incoming flow. In these and subsequent figures, the DNS data is represented by the full line, and the RANS results are given by the symbols ($\circ$ the RSM, $\square$ the $k-\omega$ SST, $\triangle$ the $k-\omega$ standard, $\triangleleft$ the S–A standard, $+$ the HYDRA S–A with the strain–vorticity correction, and $\Diamond$ the modified HYDRA S–A). Additionally, the laminar profile, resulting in the same wall shear stress as the upstream fully developed flow, is also shown for comparison. This is given by the dash-dot line. As can be seen, from the frame (a) of Fig. 2, at the upstream region, the RANS predictions conform well with the DNS. Here, the standard $k-\omega$ model results in the largest error. It is around 5%. Then, within the contraction, the tested turbulence models result in reasonable agreement with the DNS. Particularly, near the wall, the predictions match the DNS velocity gradient. These are shown in the frame (b) of Fig. 2, and the frames (a) and (b) of Fig. 3. Hereafter, without proper correction, only the RSM is able to capture the laminarisation effect. Whereas, the modified S–A model provides a close match to the DNS. The largest deviation from the DNS is around 2%.

To see this, the corresponding mean velocity profiles are recast onto the usual inner-law coordinates. These are given in the frame (a) of Fig. 5 to the frame (b) of Fig. 7 for the above streamwise locations, respectively. In these figures, the wall-normal distance and the mean velocity are scaled by the corresponding local inner values. As can be seen, overall, the laminarisation effect is lagging the acceleration – the mean velocity profile is initially brought down due to the higher friction velocity (the frame (a) of Fig. 6), and then pushed gradually back up towards the laminar profile (the frame (b) of Fig. 6, and the frames (a) and (b) of Fig. 7). In this process, without proper correction,

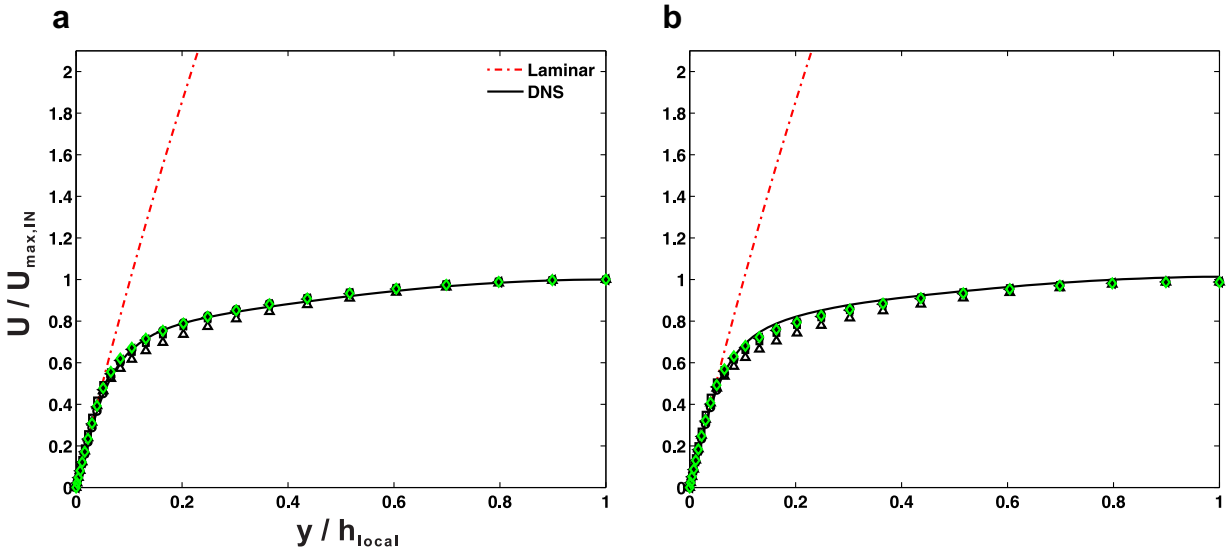

Fig. 2. Mean streamwise velocity profiles at the streamwise locations, S0 (a) and S1 (b). (– the DNS, –. the laminar, ◦ the RSM, □ the $k-\omega$ SST, △ the $k-\omega$ standard, ◁ the S–A standard, + the HYDRA S–A with the strain–vorticity correction, and ◇ the modified HYDRA S–A.)

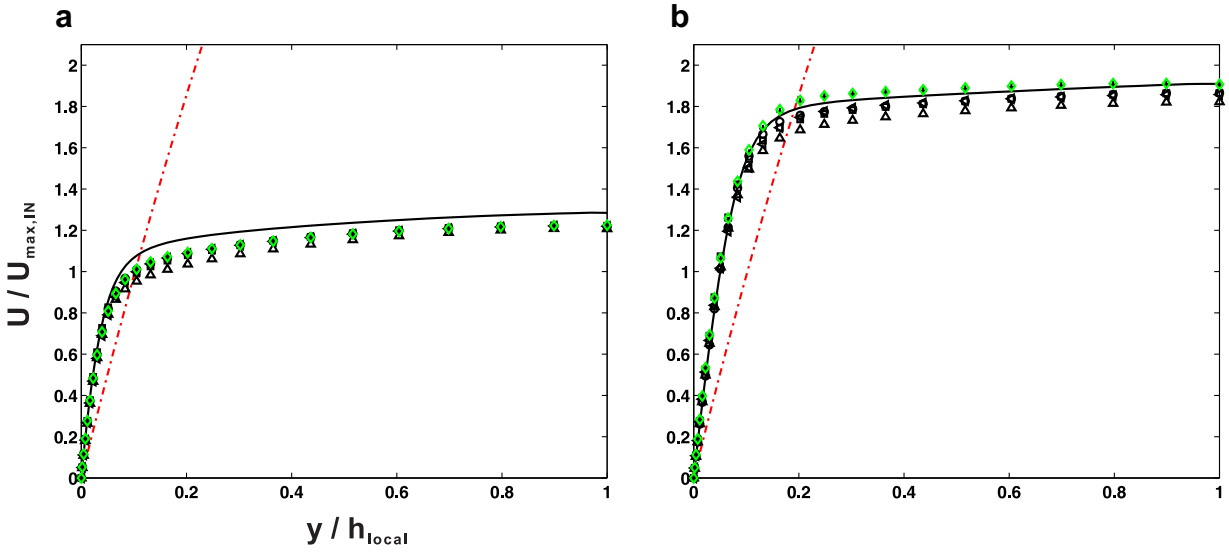

Fig. 3. Mean streamwise velocity profiles at the streamwise locations, S2 (a) and S3 (b). (– the DNS, –. the laminar, ◦ the RSM, □ the $k-\omega$ SST, △ the k–ω standard, ◁ the S–A standard, + the HYDRA S–A with the strain–vorticity correction, and ◇ the modified HYDRA S–A.)

the eddy-viscosity models produce increasingly larger discrepancies (> 20%) downstream to the contraction. This is shown in the frames (a) and (b) of Fig. 7. As can be seen, only the RSM and the modified S–A model match the DNS.

Accordingly, the streamwise distributions of the friction velocity $u_\tau = \sqrt{\tau_w/\rho}$, the skin friction coefficient $C_f = \tau_w/(0.5\rho U^2_{edge})$, and the surface pressure coefficient $C_p = (P - P_{ref})/(0.5\rho U^2_{edge})$ are compared in Fig. 8. As can be seen from the frames (a) and (b), before the end of the contraction, all the tested turbulence models predict these two viscous drag indicators, u_τ and C_f, reasonably well. The largest deviation from the DNS is around 5%. Due to the immediate recovery to the fully turbulent state, for the original eddy-viscosity models, further downstream, the predicted wall frictions are substantially higher than the DNS. Here, the relative error can be more than 50%. On the other hand, the RSM predicts the lag effect, even though the discrepancy gradually rises along with the turbulence recovery process. Here, as can be seen, the modified S–A prediction consistently mirrors the DNS behaviour. Additionally, all the RANS predictions provide similar surface pressure distributions, notwithstanding the relatively large difference from the DNS. Near the trailing edge of the contraction, the relative error is around 60%. Notably, the reference of the mean static pressure P_{ref} is taken as the surface value at the end of the examined region. Also, in this figure and the following Fig. 10, the leading and trailing edges of the contraction (S1 and S3) are indicated by the vertical dash-dot lines.

Importantly, to see the laminarisation effect to the turbulence intensity, Fig. 9 compares the TKE distributions at the aforementioned six streamwise locations. These are for the RSM, the standard k–ω, and the SST models. In this figure, the wall-normal distance is scaled by the corresponding local half-channel height, and the TKE is scaled by the corresponding local inner value. As can be seen from the first frame, for the incoming turbulence, the RANS predictions agree reasonably well with the DNS. The largest error is up to around 10%. Through the contraction, both the RSM and the two-equation models are able to reflect the turbulence reduction, even though there are quantitative discrepancies with respect to the DNS. When flow into the parallel outlet, such differences are progressively larger. The largest deviation is around 50%. For the standard k–ω

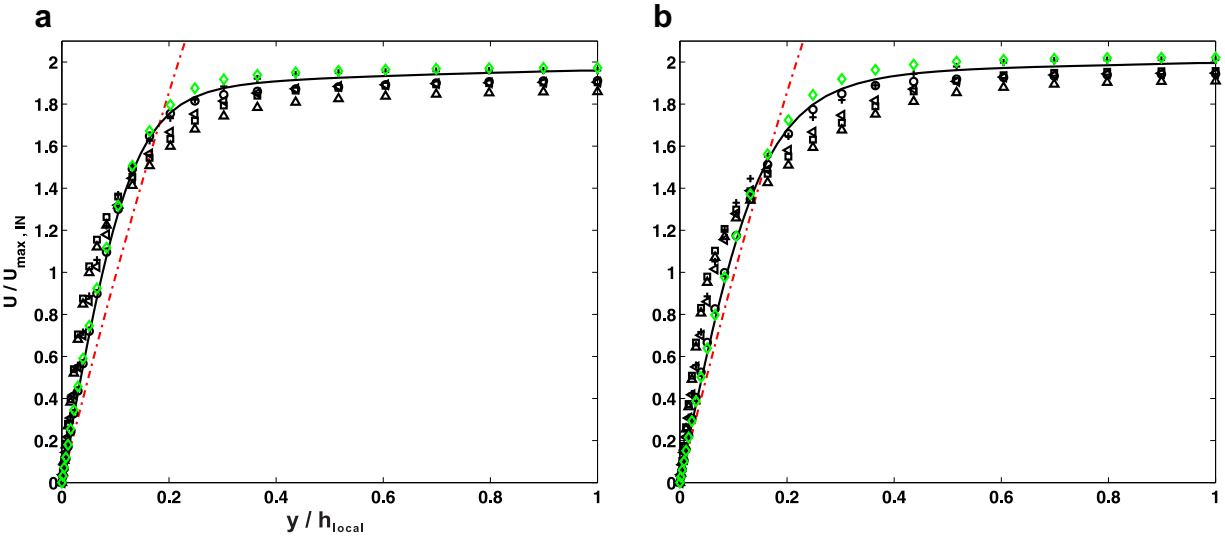

Fig. 4. Mean streamwise velocity profiles at the streamwise locations, S4 (a) and S5 (b). (– the DNS, –. the laminar, ◦ the RSM, □ the k–ω SST, △ the k–ω standard, ◁ the S–A standard, + the HYDRA S–A with the strain–vorticity correction, and ◇ the modified HYDRA S–A.)

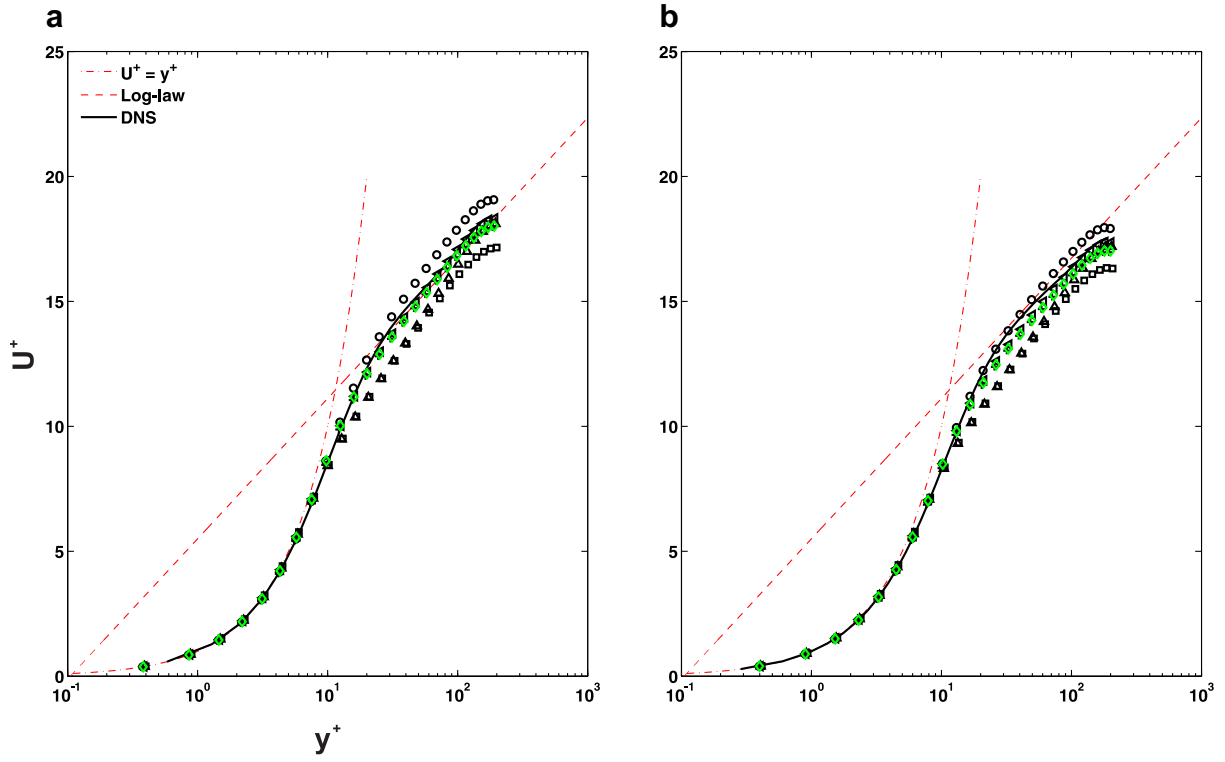

Fig. 5. Mean streamwise velocity profiles in logarithmic abscissa at the streamwise locations, S0 (a) and S1 (b). (– the DNS, ◦ the RSM, □ the k–ω SST, △ the k–ω standard, ◁ the S–A standard, + the HYDRA S–A with the strain–vorticity correction, and ◇ the modified HYDRA S–A.)

and the SST models, TKE recovers rapidly back up to the same level as the fully developed turbulence; whereas, the RSM prediction reflects the gradually recovery process, in spite of the lower growth rate.

To see this further, the corresponding streamwise distributions of the peak TKE are compared in Fig. 10, together with the distributions of the peak outer and inner scale acceleration parameters, i.e. $K_x^E = (\nu_0/U_{edge}^2) \cdot (\partial U/\partial x)$ and $K_x^+ = (\partial U/\partial x)/(\partial U/\partial y)_w$. As can be seen from frame (a), the DNS data shows that the TKE is substantially minimised through the contraction; thereafter, it progressively recovers. Evidently, both the RSM and the two k–ω models are able to capture the laminarisation mechanism through the rapid acceleration. Nevertheless, the downstream TKE production rate is too high for the two-equation models, whereas too low for the RSM. Such flow phenomena may be indicated by the acceleration parameters shown in the frames (b) and (c). Through the contraction, the mean flow experiences a substantial rapid acceleration. As can be seen from these two frames, all the tested turbulence models predict the maximum streamwise accelerations similar to that of the DNS; whereas, close to the wall, around the trailing edge of the contraction and thereafter, the mean flow slightly decelerates. This is indicated by the minimum acceleration parameters. Clearly, only the RSM and the modified S–A models accurately predict this process. The corresponding spatial distributions of the predicted K_x^E and K_x^+ are given in Figs. 11 and

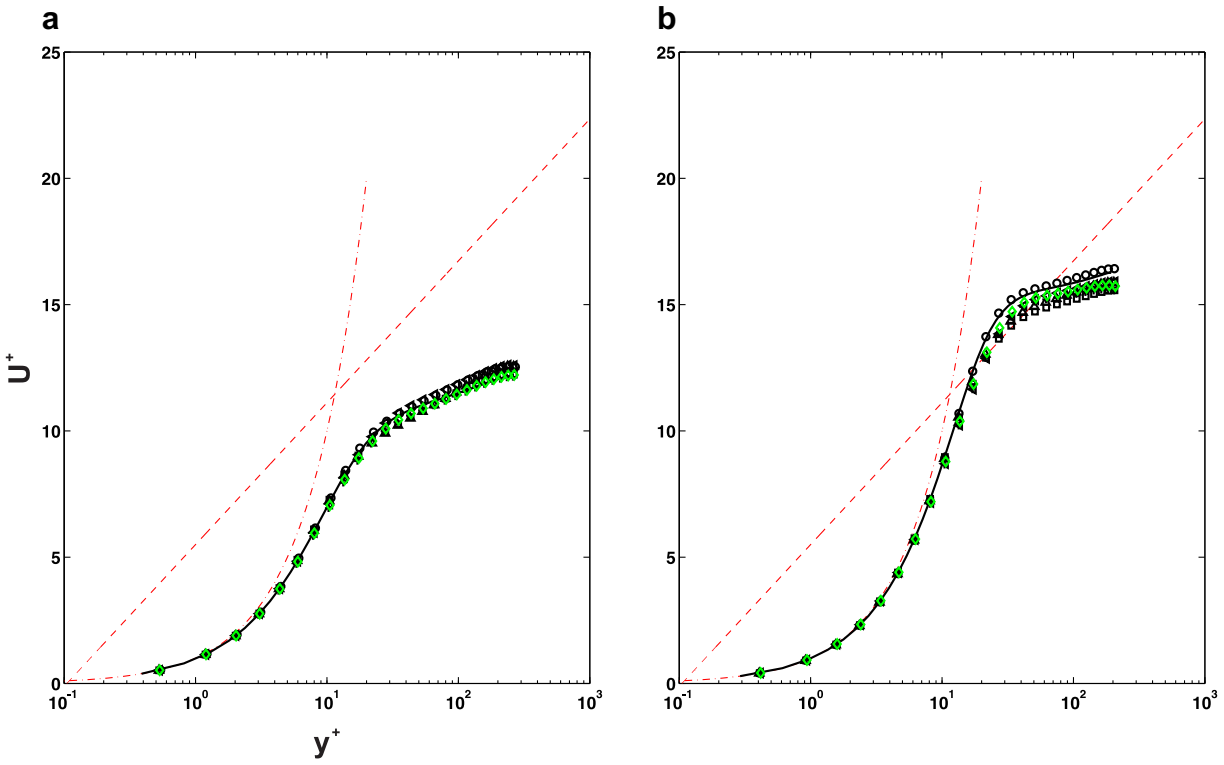

Fig. 6. Mean streamwise velocity profiles in logarithmic abscissa at the streamwise locations, S2 (a) and S3 (b). (– the DNS, ∘ the RSM, □ the k–ω SST, △ the k–ω standard, ◁ the S–A standard, + the HYDRA S–A with the strain–vorticity correction, and ◇ the modified HYDRA S–A.)

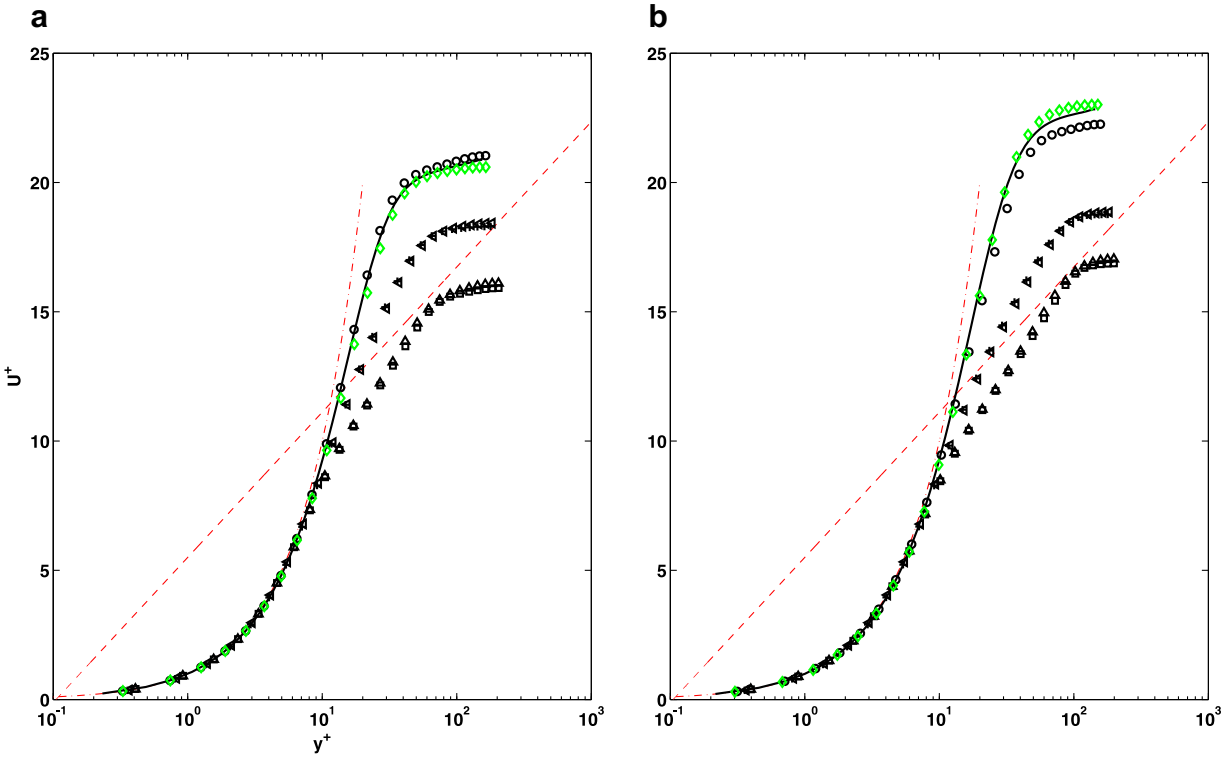

Fig. 7. Mean streamwise velocity profiles in logarithmic abscissa at the streamwise locations, S4 (a) and S5 (b). (– the DNS, ∘ the RSM, □ the k–ω SST, △ the k–ω standard, ◁ the S–A standard, + the HYDRA S–A with the strain–vorticity correction, and ◇ the modified HYDRA S–A.)

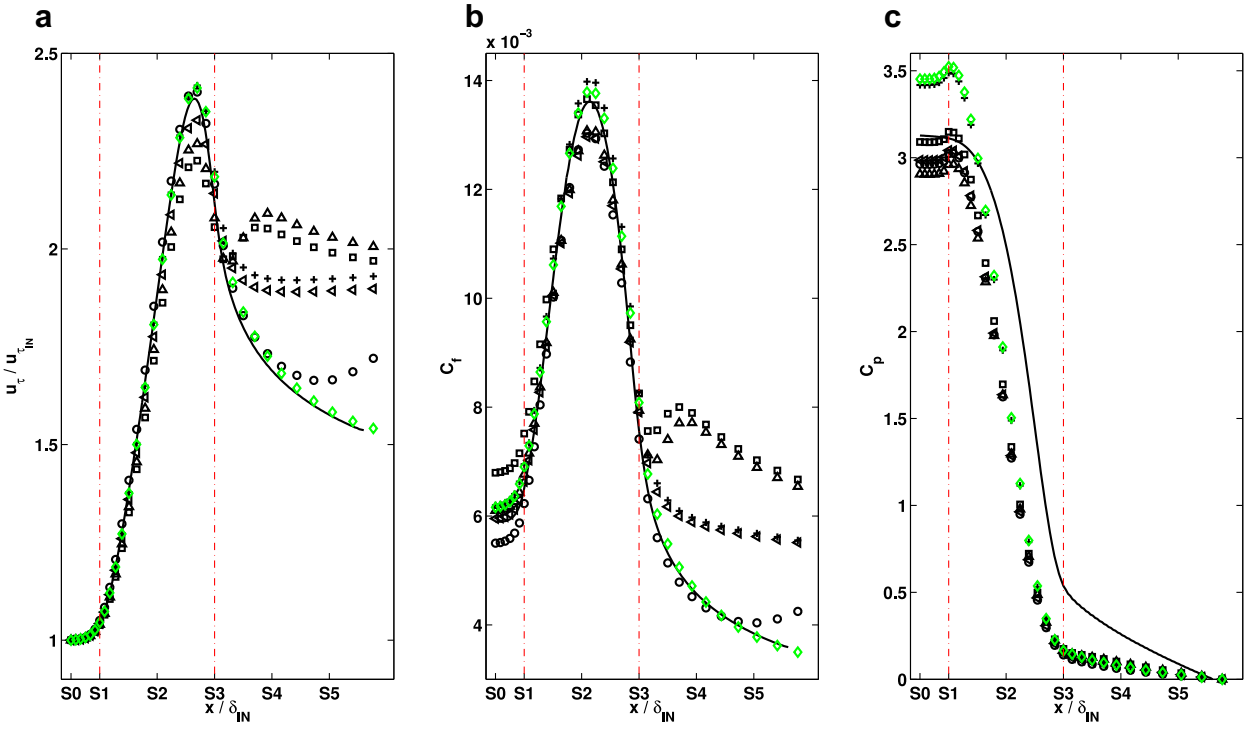

Fig. 8. Streamwise distributions of (a) $u_\tau = \sqrt{\tau_w/\rho}$, (b) $C_f = \tau_w/(0.5\rho U^2_{edge})$, and (c) $C_p = (P - P_{ref})/(0.5\rho U^2_{edge})$. (– the DNS, ○ the RSM, □ the k–ω SST, △ the k–ω standard, ◁ the S–A standard, + the HYDRA S–A with the strain–vorticity correction, and ◇ the modified HYDRA S–A.)

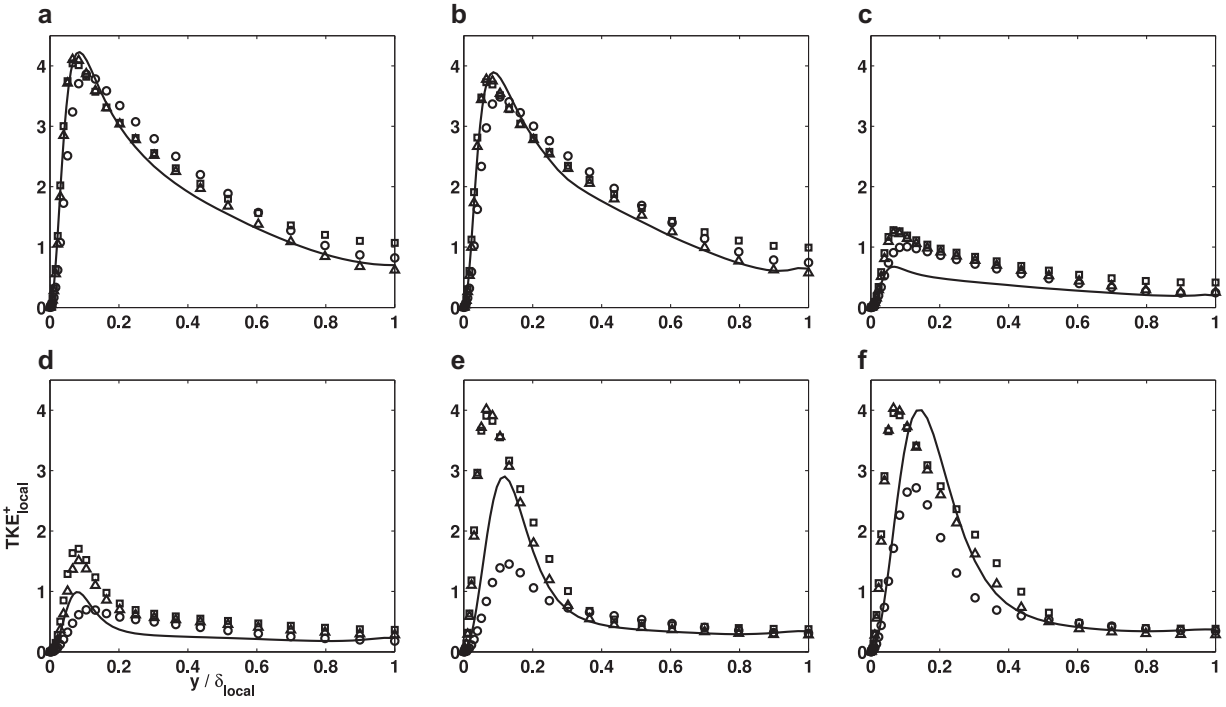

Fig. 9. Turbulence kinetic energy profiles at six streamwise locations. (a)–(f), S0 — S5. (– the DNS, ○ the RSM, □ the k–ω SST, △ the k–ω standard.)

12, respectively. Moreover, the modified S–A solutions for three of the other DNS cases are given in the Appendix.

As seen from the above, within the contraction, even though all the models predict the essential laminarisation characteristics, overall, the RSM provides the closest predictions to the DNS. However, further downstream when the acceleration or essentially the substantial favourable pressure gradient is removed, larger discrepancies arise for the predicted turbulence recovery. As has been shown [33], in addition to the anisotropic turbulence recovery, for the mean velocity, the laminarisation effect is lagging to the acceleration. To certain degree, these progressive changes are predicted by the RSM. The eddy-viscosity models tend to return the flow immediately back to fully turbulent; necessarily, some form of the lag modelling is needed. Based on this, an acceleration extension has been proposed for the S–A model, i.e. Eq. (2) with $\sigma^a_{K_s} = 0$ and $\sigma^b_{K_s} = 0.1$ for the region downstream of a severe acceleration. This new model is

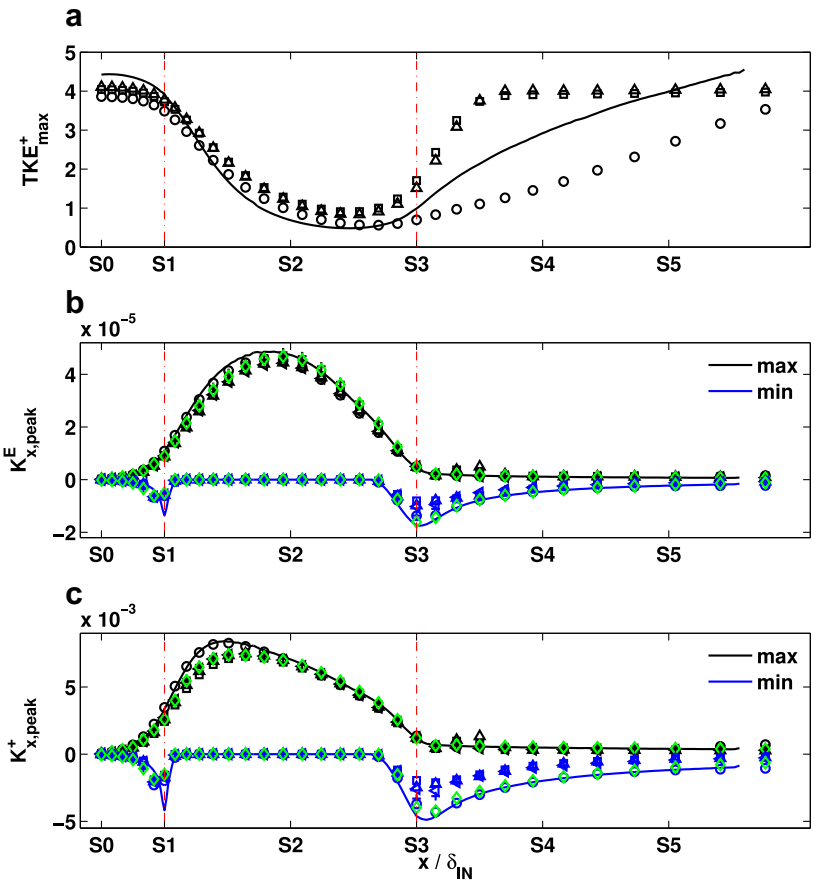

Fig. 10. Streamwise distributions of (a) the peak TKE, and (b, c) the peak mean streamwise acceleration parameter in the outer and inner scales, i.e. $K_x^E = (\nu_0/U_{edge}^2)\cdot(\partial U/\partial x)$ and $K_x^+ = (\partial U/\partial x)/(\partial U/\partial y)_w$. (− the DNS, ○ the RSM, □ the k–ω SST, △ the k–ω standard, ◁ the S–A standard, + the HYDRA S–A with the strain–vorticity correction, and ◇ the modified HYDRA S–A.)

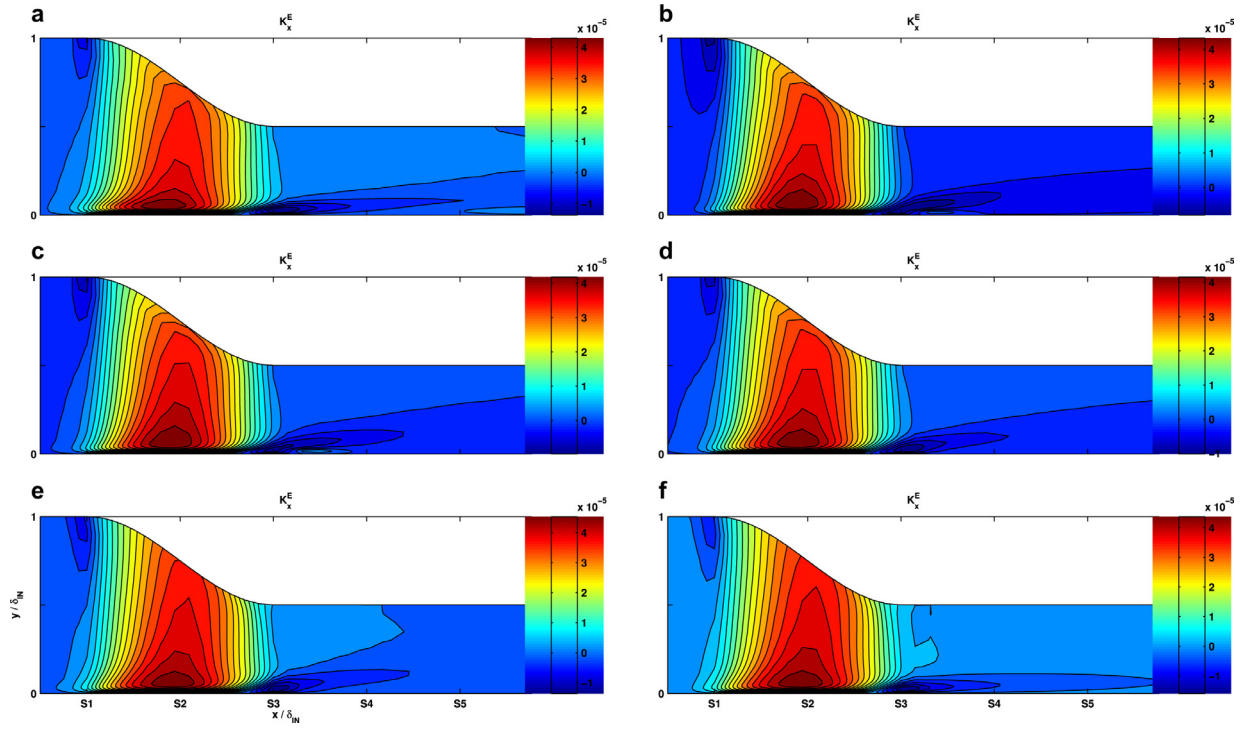

Fig. 11. Spatial distributions of the mean streamwise acceleration parameter $K_x^E = (\nu_0/U_{edge}^2)\cdot(\partial U/\partial x)$. (The frames (a)–(f) are for the predictions using the RSM, the SST and the standard k–ω models, the standard S–A model and the HYDRA S–A with the strain–vorticity correction, and also the modified HYDRA S–A model, respectively.)

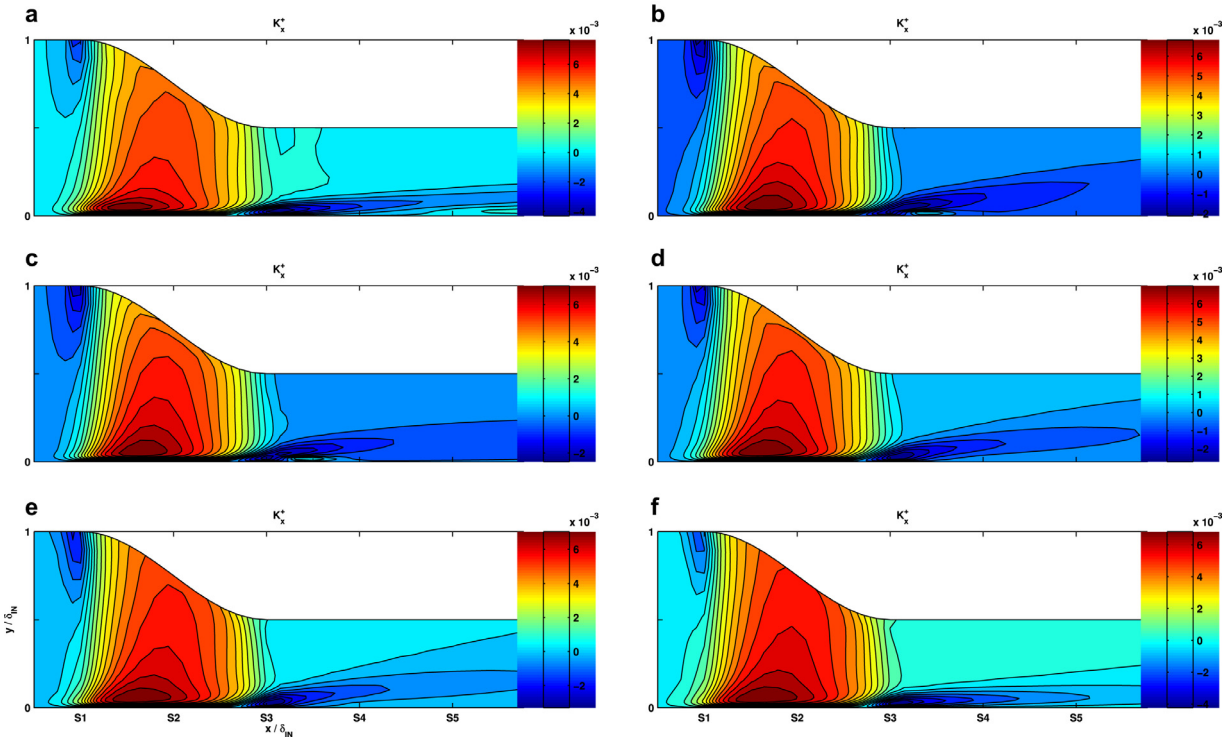

Fig. 12. Spatial distributions of the mean streamwise acceleration parameter $K_x^+ = (\partial U/\partial x)/(\partial U/\partial y)_w$. (The frames (a)–(f) are for the predictions using the RSM, the SST and the standard k–ω models, the standard S–A model and the HYDRA S–A with the strain–vorticity correction, and also the modified HYDRA S–A model, respectively.)

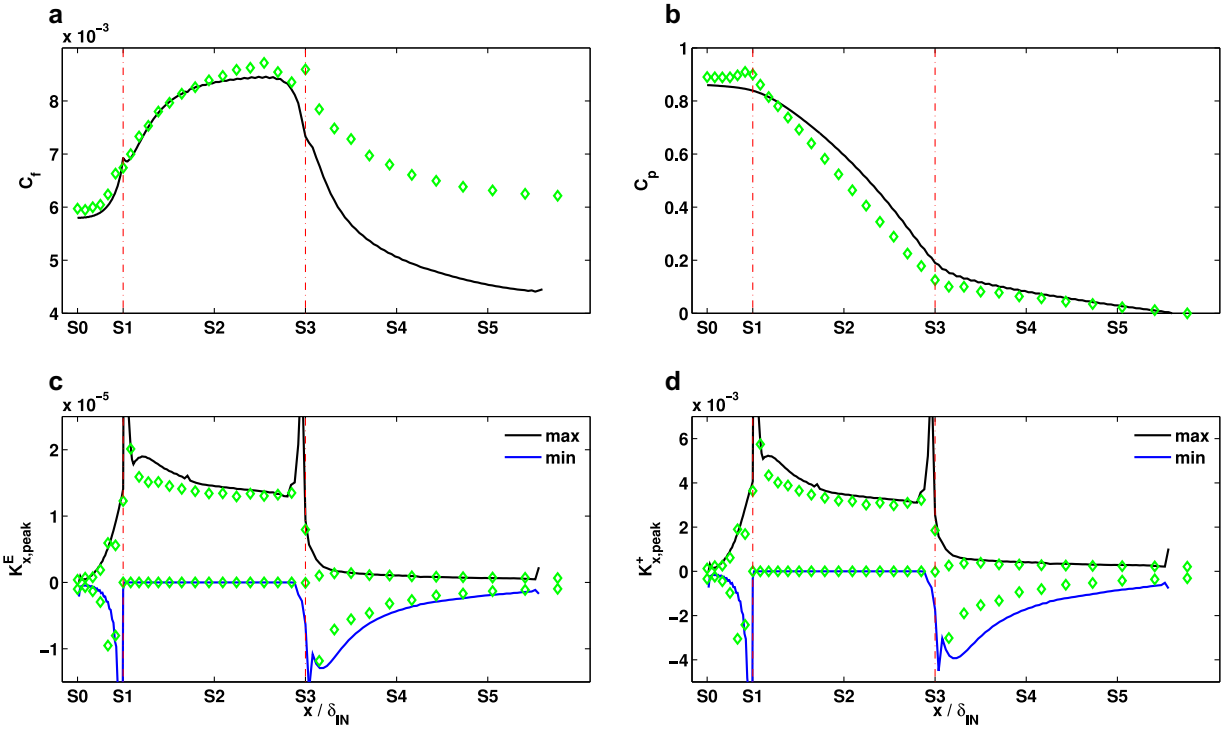

Fig. 13. HYDRA RANS (the S–A model with the strain–vorticity correction) solutions for the 2D contraction channel flow. These are the modified S–A solutions for the Case I(a).

essentially inspired by the hypothesis that the highly accelerated turbulence is in a frozen state as proposed by Launder and Jones [1]. As shown above, the modified solutions match the corresponding mean flow characteristics of the DNS.

Finally, as shown [33], in the absence of pressure redistributions, the downstream turbulence recovery is largely streamwise dominant. Importantly, in this process, the production rate P_{12}^+ of the Reynolds shear stress $\overline{u'v'}$ is fairly small. This in turn renders a relatively slow recovery rate for $-\overline{u'v'}$ and essentially the TKE production through the parallel outlet. Accordingly, this contradicts the approximation $-\overline{u'v'} = \nu_t(\partial U/\partial y)$. Hence, for this region, the Boussinesq approximation is questionable. This is considered as the reason why the

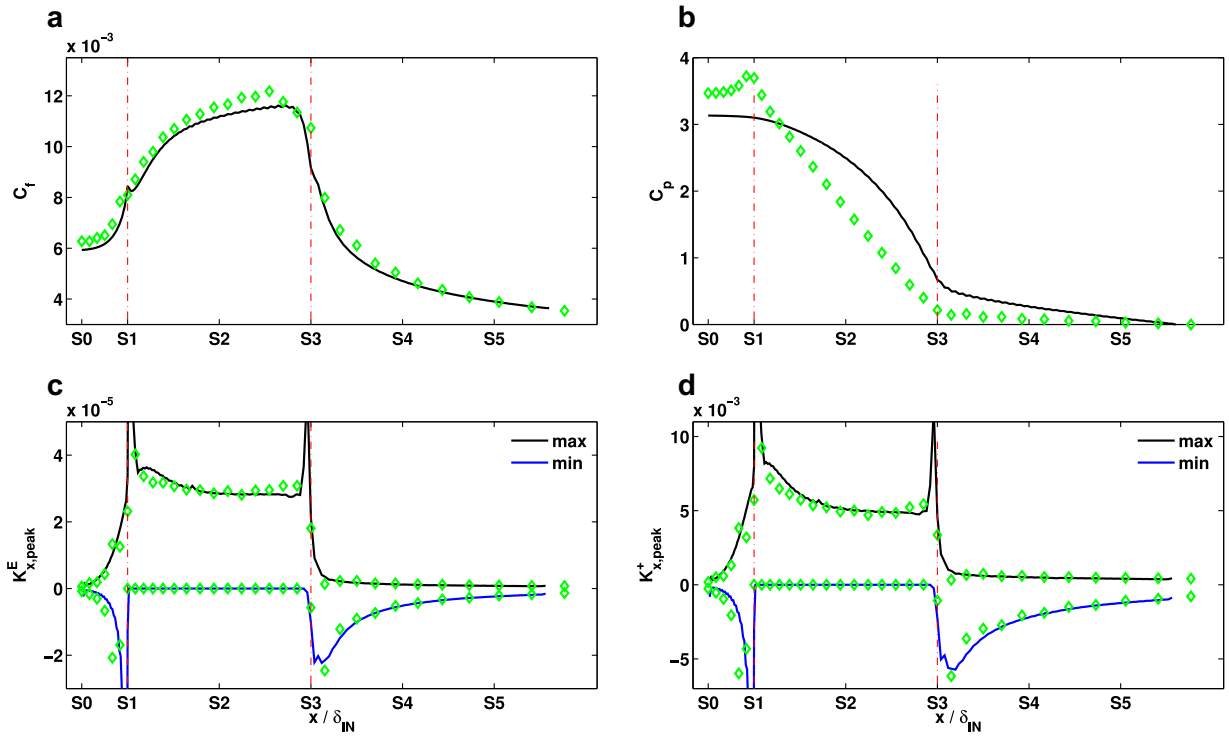

Fig. 14. HYDRA RANS (the S–A model with the strain–vorticity correction) solutions for the 2D contraction channel flow. These are the modified S–A solutions for the Case I(b).

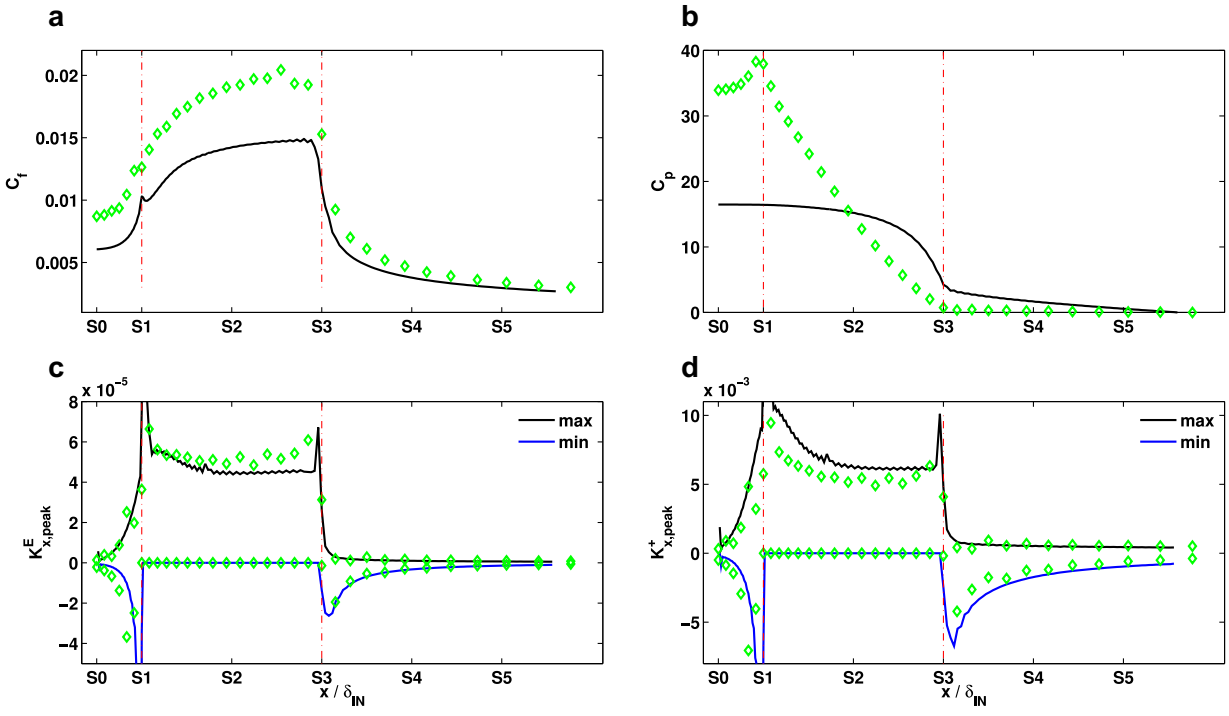

Fig. 15. HYDRA RANS (the S–A model with the strain–vorticity correction) solutions for the 2D contraction channel flow. These are the modified S–A solutions for the Case I(c).

standard $k-\omega$ and the SST models produce the rapid return to the fully developed turbulence. Accordingly, through the rapid acceleration, the pressure redistribution terms Π_{ij} for the Reynolds stresses vanish promptly. This is the primary reason for the substantial anisotropic turbulence recovery. Whereas, for the RSM with the stress–ω formulation, the approximated pressure–strain correlation is only justifiable for homogeneous turbulence that is near equilibrium [39,40]. Primarily, it is considered that this leads to the predicted lower TKE recovering rate than the DNS.

5. Conclusion

To assess turbulence model performance with improved turbulence modelling in mind, RANS predictions have been performed for turbulent channel flows experiencing a rapid contraction, using some popular RSM and eddy-viscosity models. These available models include the second-order closure with the stress–ω formulation, the standard $k-\omega$ and the SST models, the standard S–A model with and without the strain–vorticity correction. As shown, prior to

the end of the contraction, all the benchmarked models predict the mean flow characteristics close to those of the DNS. However, further downstream, the discrepancies gradually increase. According to the DNS data, the laminarisation effects are lagging to the acceleration. Also, through the downstream parallel outlet, turbulence is progressively recovered but into the streamwise dominant structures. Without proper corrections, only the RSM provides reasonably accurate predictions for the mean flow, even though the downstream TKE recovering rate is lower than that of the DNS. In contrary, the eddy-viscosity models tend to return the flow immediately back to the fully developed turbulence. For this, an acceleration extension for the S–A model is proposed based on the frozen state hypothesis. The corresponding modified predictions match those of the DNS. Moreover, as seen, the sensitisation to the impact of the large integral length scales would be beneficial for all models.

Acknowledgments

The authors would like to acknowledge the EPSRC and Rolls Royce for their financial support, as well as the U.K. Turbulence Consortium. They would also like to thank all their colleagues at the University of Cambridge, especially Prof. Stewart Cant, Dr. Richard J. Jefferson-Loveday, Dr. Martin N. Goodhand, Dr. Nagabhushana Rao Vadlamani, Dr. Ugochukwu R. Oriji, and Dr. Iftekhar Z. Naqavi for their contributions to the research.

Appendix

The modified S–A solutions for the two-dimensional contraction channel flow are given in this appendix (Figs. 13,14,15). These are the Case I(a), I(b), and I(c) with a straight contraction shape [33]. The contraction ratios h_4/h_1 for these cases are 0.75, 0.5, and 0.25; the corresponding peak acceleration parameters $K^E_{x,max}$ are 1.899×10^{-5}, 3.633×10^{-5}, and 5.594×10^{-5}, individually. Also, the contraction length is the same as the above Case I(x), i.e. $L_3 = 2\pi\delta$. The detailed descriptions on the acceleration extension for the S–A model, the numerical procedure, and the corresponding flow configurations have been given in the previous sections. For each case, the compared results include the skin friction coefficient C_f, the surface pressure coefficient C_p, and the peak values of the outer and inner scale acceleration parameters K^E_x and K^+_x. The DNS data are given by the full line and the symbols are for the S–A predictions. Notably, as can be seen from Fig. 13, the relatively large differences for the Case I(a), with respect to the DNS data, are caused by the weak laminarisation.

References

[1] Launder BE, Jones WP. On the prediction of laminarisation. C.P. No. 1036. Ministry of Technology, Aeronautical Research Council; 1969.
[2] Launder BE, Jones WP. Sink flow turbulent boundary layer. J Fluid Mech 1969;38:817–31.
[3] Schraub FA, Kline SJ. A study of the structure of the turbulent boundary layer with and without longitudinal pressure gradients. Thermoscience Division Report MD-12. Stanford University; 1965.
[4] Moretti PM, Kays WM. Heat transfer through an incompressible turbulent boundary layer with varying free-stream velocity and varying surface temperature. Report No PG-1. Mechanical Engineering Department, Stanford University; 1965.
[5] Patel VC. Calibration of the Preston tube and limitations on its use in pressure gradient. J Fluid Mech 1965;23:185.
[6] Patel VC. Contributions to the study of turbulent boundary layers [Ph.D. thesis]. University of Cambridge; 1965.
[7] Patel VC, Head MR. Reversion of turbulent to laminar flow. J Fluid Mech 1968;34:371–92.
[8] Badri Narayanan MA. An experimental study of the decay of non-isotropic turbulence in two-dimensional channel flow. J Fluid Mech 1966;31:609.
[9] badri Narayanan MA, Ramjee V. On the criteria for reverse transition in a two-dimensional boundary layer flow. Report AE 68 FM 1. Indian Institute of Science, Bangalore; 1968.
[10] badri Narayanan MA, Ramjee V. On the criteria for reverse transition in a two-dimensional boundary layer flow. J Fluid Mech 1969;35:225–41.
[11] Moretti PM, Kays WM. Heat transfer to a turbulent boundary layer with varying free-stream velocity and varying surface temperature. International Journal of Heat and Mass Transfer 1965;8:1187.
[12] Sergienko AA, Gretsov VK. Transition from a turbulent to a laminar boundary layer. RAE Translation No. 827; 1959.[Translation from Russian].
[13] Launder BE. Laminarisation of the turbulent boundary layer by acceleration. Report No. 77. MIT Gas Turbine Laboratory; 1964.
[14] Launder BE. Laminarisation of the turbulent boundary layer in a severe acceleration. J Appl Mech 1964;31:707.
[15] Jones WP. Strongly accelerated turbulent boundary layers [M.Sc. thesis]. London: Imperial College; 1967.
[16] Launder BE, Stinchcombe HS. Non-normal similar boundary layers. Report TWF/TN/21. Imperial College, Mechanical Engineering Department; 1967.
[17] Jones WP, Launder BE. Some properties of sink-flow turbulent boundary layers. J Fluid Mech 1972;56:337–51.
[18] Spalart PR. Numerical study of sink-flow boundary layers. J Fluid Mech 1986;172:307–28.
[19] Prandtl L. Bericht uber Untersuchungen zur ausgebildeten turbulenz. Z angew Math Mech 1925;5:136.
[20] Prandtl L. Uber eine neues formelsystem fur die ausgebildete turbulenz. Nachr Akad Wiss Gottingen Mathphys 1945:16.
[21] van Driest ER. On turbulent flow near a wall. J Aerosp Sci 1956;23:1007.
[22] Kays WM, Moffat RJ, Thielbahr. Heat transfer to the highly accelerated turbulent boundary layer with and without mass addition. Journal of Heat Transfer 1970.
[23] Cebeci T, Mosinskis GJ. Predictions of turbulent boundary layers with mass addition including highlyaccelerating flows. J Heat Transf 1971;93(3):271–80.
[24] Powell TE, Strong AB. Calculations of the two-dimensional turbulent boundary layer with mass addition and heat transfer. In: Proceedings of the Heat Transfer and Fluid Mech Institute. Stanford University; 1970.
[25] Jones WP, Launder BE. The prediction of laminarization with a two-equation model of turbulence. Int J Heat Mass Transf 1972;15:301–14.
[26] Launder BE, Spalding DB. Lectures in mathematical models of turbulence. London, England: Academic Press; 1972.
[27] Launder BE, Spalding DB. The numerical computation of turbulent flows. Comput Methods Appl Mech Eng 1974;3:269–89.
[28] Hanjalic K, Launder BE. A Reynolds stress model of turbulence and its application to thin shear flows. J Fluid Mech 1972;52:609–38.
[29] Hanjalic K, Launder BE. Contribution towards a Reynolds-stress closure for low-Reynolds-number turbulence. J Fluid Mech 1976;74:593–610.
[30] Piomelli U, Yuan J. Numerical simulations of spatially developing, accelerating boundary layers. Phys Fluids 2013;25:101304-1–101304-21.
[31] Karimisani S, Oriji UR, Tucker PG. RANS modelling of accelerating boundary layers. In: Proceedings of the ASME 2013 international mechanical engineering congress and exposition, IMECE2013-63467, November 15–21, 2013, San Diego, California, USA; 2013.
[32] Oriji UR, Tucker PG. Modular turbulence modelling applied to an engine intake. J Turbomach 2013;136:051004.
[33] Xiaoyu Yang. Numerical investigation of turbulent channel flow subject to surface roughness, acceleration, and streamline curvature [Ph.D. thesis]. Department of Engineering, University of Cambridge; 2014.
[34] Lapworth L, Shahpar S. Design of gas turbine engines using CFD. In: Proceedings of the European congress on computational methods in applied sciences and engineering, ECCOMAS; 2004.
[35] Lapworth L. The challenges for aero-engine CFD. In: Proceedings of the ICFD 25th anniversary meeting, Derby, UK; 2008.
[36] ANSYS. FLUENT theory guide. Southpointe, Canonsburg, PA 15317, USA: ANSYS Inc.; 2011.
[37] Yang X, Tucker PG. Assessment of turbulence model performance: Large streamline curvature and integral length scales. Comput Fluids 2016;126:91–101.
[38] Spalart PR, Allmaras SR. A one-equation turbulence model for aerodynamics flows. La Rech Aerosp 1994;1:5–21.
[39] Speziale CG. A review of Reynolds stress models for turbulent shear flows, ICASE Report No. 95-15. NASA-CR-195054. NASA; 1995.
[40] Speziale CG, Xu XH. Towards the development of second-order closure models for nonequilibrium turbulent flows. Int J Heat Fluid Flow 1996;17:238–44.